

Transport properties of overheated electrons trapped on a helium surface

Fabien Closa^{1,2}, Elie Raphaël¹, and Alexei D. Chepelianskii^{3,a}

¹ Laboratoire de Physico-Chimie Théorique, UMR CNRS Gulliver 7083, ESPCI, 75005 Paris, France

² Laboratoire de Physique Théorique de la Matière Condensée, UMR 7600 LPTMC, 4 place Jussieu, 75252 Paris Cedex 05, France

³ Cavendish Laboratory, University of Cambridge, J.J. Thomson Avenue, Cambridge CB3 0HE, UK

Received 16 April 2014 / Received in final form 6 June 2014

Published online 11 August 2014 – © EDP Sciences, Società Italiana di Fisica, Springer-Verlag 2014

Abstract. An ultra-strong photovoltaic effect has recently been reported for electrons trapped on a liquid helium surface under a microwave excitation tuned at intersubband resonance [D. Konstantinov, A.D. Chepelianskii, K. Kono, J. Phys. Soc. Jpn **81**, 093601 (2012)]. In this article, we analyze theoretically the redistribution of the electron density induced by an overheating of the surface electrons under irradiation, and obtain quantitative predictions for the photocurrent dependence on the effective electron temperature and confinement voltages. We show that the photo-current can change sign as a function of the parameters of the electrostatic confinement potential on the surface, while the photocurrent measurements reported so far have been performed only at a fixed confinement potential. The experimental observation of this sign reversal could provide a reliable estimation of the electron effective temperature in this new out of equilibrium state. Finally, we have also considered the effect of the temperature on the outcome of capacitive transport measurement techniques. These investigations led us to develop, numerical and analytical methods for solving the Poisson-Boltzmann equation in the limit of very low temperatures which could be useful for other systems.

Electrons trapped on the liquid helium surface were the first experimental realization of a high mobility two-dimensional conductor [1,2]. The extremely high mobility of the surface electrons allows to explore in a unique way many problems in fundamental physics, examples include Wigner crystallization [3], propagation of magnetoplasmon waves [4,5], transport of correlated charges in confined geometries [6,7], quantum melting [8] and sliding [9,10]. The interest in this system has been renewed by its potential for quantum computation that comes from their very large spin coherence times [11] and from the spacial addressability of the electrons on the surface [12,13]. Recently, an unexpected transport regime was observed in novel experiments where surface electrons were excited by a millimeter-wave irradiation [14,15]. This regime occurs when the perpendicular magnetic field lies within regularly spaced intervals for which the ratio between the microwave and cyclotron frequencies is close to an integer value. It also appears only when the photon energy is equal to the energy spacing between the two lowest transport subbands. This transition is usually called intersubband resonance, it corresponds to transitions between the ground state and the first excited state of the electronic wavefunction in the direction perpendicular to the helium surface. Once the above conditions on the perpendicular magnetic field and on the photon-energy are sat-

isfied, the irradiation can lead to a complete suppression of the dissipative component of the electronic response in capacitive measurements. This effect is strikingly similar to zero-resistance states that were first reported in ultra high mobility GaAlAs hetero-structures [16,17].

Further experiments on surface electrons showed a strong redistribution of the electronic density compared to its equilibrium shape under zero-resistance conditions [18]. This redistribution was characterized by a depletion of the electronic density at the center of the electron cloud and by an accumulation of electrons towards the edge of the cloud. One of the motivations for these experiments was the possibility of electron trapping at the edges of the system under microwave irradiation that has been proposed theoretically [19] and confirmed recently in extensive numerical simulations [20]. However other mechanisms could also be responsible for this redistribution. Indeed, a theoretical description of the magneto-resistance oscillations under irradiation has recently been proposed by Monarkha [21,22]. Although this theory does not directly predict a redistribution of the electronic density similar to that observed in the experiments, it has been suggested that such a redistribution could occur, due to the instability of the negative resistance state that appears in this theory [23]. Finally a strong overheating of the surface electrons could also result in a significant redistribution of the electronic density. In order to distinguish between these different mechanisms that compete with each

^a e-mail: alexei.chepelianskii@gmail.com

other we analyze theoretically the overheating scenario in the present article. We show that in this case the direction of the photo-current can be reversed by changing the confinement gate potentials, a behavior which is not expected for other redistribution mechanisms and that could thus be important to determine the out-of-equilibrium electron temperature.

When surface electrons (SE) absorb microwave irradiation their effective temperature can increase significantly above the temperature of the helium bath. At zero magnetic field, the effective temperature of the electrons under microwave pumping of the intersubband resonance was studied both theoretically and experimentally in reference [24]. It was shown that electrons could be overheated to temperatures in the range of $T_e \simeq 10$ K even if the temperature of the helium bath was much lower $T_0 \simeq 0.3$ K, however no estimation of T_e is available in the zero resistance state (ZRS) regime. Experimentally it was shown that the formation of ZRS is accompanied by a strong redistribution of the electrons on the helium surface, which can cost up to a 100 meV charging energy per electron [18]. Thus the electrons need to absorb many microwave photons (typical frequencies are in the 100 GHz range) to store the needed energy, which suggests that they can occupy highly excited states. It is probable that their energy distribution cannot be described appropriately by an effective temperature in this regime. However, since this is the simplest starting model to understand the distribution of the electrons under irradiation, we have investigated the effect of a high electron temperature on the electron density profile $n_e(\mathbf{r})$ in the trapping potential. As the charging energy cost is surprisingly high we are led to consider temperatures much larger than the thermal energy of the bath, we note however that these temperatures are still an order of magnitude lower than the penetration barrier into the liquid helium or than the height of the confining potentials which are both in the eV range.

Finally as a further motivation for our investigations, we developed a Monte-Carlo method which allows to solve the Poisson-Boltzmann equation in the limit of very low temperatures where the applied voltages exceed T_e by several orders of magnitude. Conventional finite elements relaxation techniques perform very poorly in this regime where the convection term of the electron flow strongly dominates the diffusive electron current. We thus believe that the methods developed here can be useful for other physical problems where the Poisson-Boltzmann equation is relevant. It is worth emphasising here that we have previously studied a problem on counterion-condensation around hydrophobic globules which is mathematically very similar to the problem of finding the equilibrium electronic density at finite temperatures [25,26].

1 Simulation of hot electron density distribution

Since SE form a non degenerate system, their distribution on the surface is governed by a Boltzmann statistics at

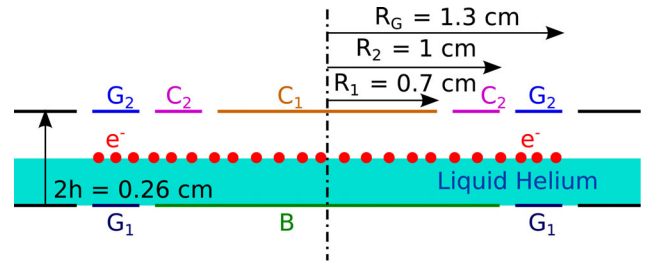


Fig. 1. Schematic diagram of the experimental cell modeled in our simulations. The cell is cylindrically symmetric, surface electrons are trapped above the central disc electrode B and the bottom guard electrode G_1 . The potential of B was fixed to $V_B = 4.2$ V in all the simulations (a typical experimental value). Electrodes C_2 and C_1 are grounded, except in section IV where a small AC potential is applied to C_1 . In all simulations the potential difference between G_1 and G_2 is fixed to V_B for reasons that are explained in the text. The voltage V_{G1} is thus the main control parameter for the shape of the electron cloud.

the electron temperature T_e :

$$n_e(\mathbf{r}) = \frac{N_e}{\int d^2\mathbf{r}' \exp\left(\frac{eV(\mathbf{r}')}{k_B T_e}\right)} \exp\left(\frac{eV(\mathbf{r})}{k_B T_e}\right). \quad (1)$$

Here e is the absolute value of the electron charge, $V(\mathbf{r})$ the electrostatic potential created by the confining electrodes and the electron cloud. The quantity N_e is the total number of electrons trapped in the cloud. The electrostatic potential $V(\mathbf{r})$ is determined by solving the Poisson equation in a cylindrical cell that is sketched in Figure 1. The potential and electron density depend only on the distance r to the cell axis and the potential $V(\mathbf{r})$ can be expressed in the following form:

$$V(r) = V_{ext}(r) + \int G(r, r') n_e(r') 2\pi r' dr' \quad (2)$$

where $V_{ext}(r)$ is the potential created by the confining electrodes alone, in absence of the electron cloud, and $G(r, r')$ a Green-function giving the potential created by electrons located at radius r' . Analytic formulas for $V_{ext}(r)$ and the Green-function are derived in the Appendix for the case where the effect of the finite radius of the experimental cell can be neglected (note also that the electrostatics of surface electrons has been analyzed in Refs. [27,28]). This approximation is accurate in the limit where the difference between the radius of the experimental cell and the radius of the electron cloud is larger than the cell height $2h$ (see Fig. 1). Finite elements simulations in a more realistic geometry confirmed that finite cell size effects are expected to be negligible in the experimental geometry used in references [14,15,18]. We also assumed that the electron density distribution remains two-dimensional even for hot electrons which is accurate as long as the electron temperature remains much smaller than the potential difference between top and bottom electrodes. Indeed in this limit the thickness of the electron cloud is still negligible before the height of the cell $2h$. The Appendix gives an explicit analytic formula

for the potential $V_{ext}(r)$ as a function of the potential of the bottom disc B and guard electrodes $G_{1,2}$ under the assumptions that were indicated above. The combination of equations (1) and (2), forms a Poisson-Boltzmann equation that needs to be solved in order to determine the electron density $n_e(r)$ and the electrostatic potential $V(r)$.

The numerical solution of this equation in the limit of low (but finite) temperatures is challenging since small errors on the value of the potential $V(r)$ can lead to a large error on the electron density $n_e(r)$ as a consequence of equation (1). This can introduce instabilities in many numerical procedures (for example direct iteration of equations (1) and (2) or relaxation methods based on drift-diffusion equations). From our numerical experiments, we found that the best stability at low temperatures was achieved by a Monte-Carlo computational method.

In this method, an ensemble of $N_t \simeq 10^4$ trial particles were displaced on the simulated region of the helium surface, using a Metropolis algorithm in the potential landscape given by equation (2). The unknown density $n_e(r)$ that appears in this equation was determined by averaging over time the probability of presence of the trial particles in thin circular shells in which the surface of the electron cloud was separated (typically the available configuration space was divided into 100 circular shells). The outlined numerical method was stable for temperatures as low as $T_e = 0.1$ K, convergence was checked by computing the relative error:

$$\epsilon_{err} = \frac{1}{N_e} \int \left| n_e(r) - \frac{N_e}{Z} \exp\left(\frac{eV(\mathbf{r})}{k_B T_e}\right) \right| d^2\mathbf{r} \quad (3)$$

with $Z = \int d^2\mathbf{r}' \exp\left(\frac{eV(\mathbf{r}')}{k_B T_e}\right)$ the normalization factor in the Boltzmann-distribution. In this expression the potential $V(\mathbf{r})$ was computed by numerical integration of equation (2) for the electron density obtained from the Monte-Carlo algorithm. Note that a more detailed description of the numerical method that we used here will be published elsewhere [29]. The value of this relative error parameter in our simulations was around $\epsilon_{err} \simeq 10^{-3}$ at high temperatures ($T_e \simeq 100$ K), $\epsilon_{err} \simeq 5 \times 10^{-3}$ at $T_e \simeq 1$ K and $\epsilon_{err} \simeq 4 \times 10^{-2}$ at the lowest temperatures $T_e \simeq 0.1$ K; as discussed above ϵ_{err} is higher at low temperatures due to the longer convergence times.

Typical electron density distributions are shown in Figure 2 for several values of the gate parameters for $N_e = 10^6$ electrons in the cloud. As the potential in the guard electrodes is increased we observe a transition between different shapes of the electron cloud. In the limit of a low potential on the guard electrodes, the electrons are confined in the central region of the cell below the electrode C_1 and the shape of the electron cloud is described by a monotonic distribution where the density vanishes at large radius r . This case corresponds to the curves at $V_{G1} = 3$ V which are represented in Figure 2. The value of the bias voltage between the guard G_1 and the disc B is then $V_{G1} - V_B = -1.2$ V. As in the experiments, a potential is also applied to the top guard electrode G_2 in order to enforce the relation $V_{G1} - V_{G2} = V_B = 4.2$ V. This constraint allows to keep the perpendicular component of the

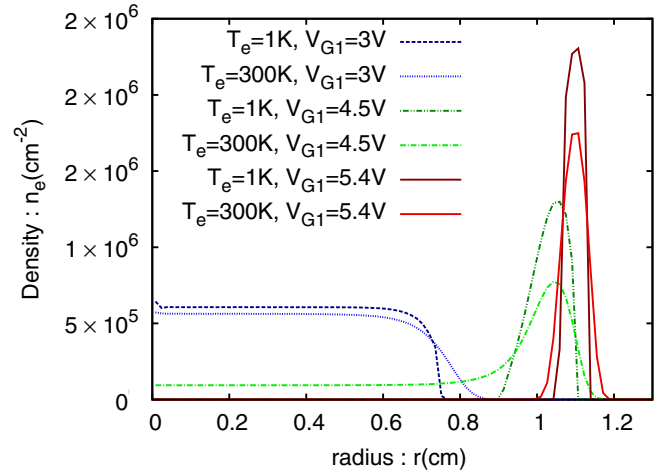


Fig. 2. Electronic density profiles $n_e(r)$ at the liquid helium surface as a function of the radius r from the center of the cell, represented at two different electron temperatures ($T_e = 1$ K and $T_e = 300$ K) and for different potentials of the electrode G_1 ($V_{G1} = 3$ V: blue curves; 5 V: green curves and 5.4 V: red curves) with a fixed total number of electrons $N_e = 10^6$. The potential of the lower central electrode B is $V_B = 4.2$ V.

electric field constant across the cell which is important to keep the same intersubband transition energy for all the electrons in the system. The second type of electron configuration occurs when the potential of the peripheral electrode V_{G1} is much higher than V_B , the electrons are then confined only above the guard electrode G_1 , forming a ring (see the curves at $V_{G1} = 5.4$ V Fig. 2). Finally an intermediate case appears when the Coulomb repulsion between electrons or their thermal energy is sufficiently strong to overcome the energy barrier created by the positive bias potential $V_{G1} - V_B$. In this case the electrons are mainly confined under the electrode G_2 but a part of the electrons density is also localized above the central electrode B forming a non-monotonic disk shaped distribution $n_e(r)$. This case is represented in Figure 2 for $V_{G1} = 4.5$ V and $T_e = 1$ K or 300 K. Note the transition between a ring shaped density to a non-monotonic disk which is observed when temperature increases at $V_{G1} = 4.5$ V.

The comparison between low and high temperature curves for these three cases reveals the following trend. In the case of a monotonic ring density the electron cloud tends to expand outwards as the electrons are heated, however when electrons form a non-monotonic disc density the trend is reversed and the electrons tend to come back towards the center as T_e increases. This effect can be qualitatively understood as the tendency of the electron temperature to smooth the electron density profile in the cloud.

In order to study quantitatively the effects of electron heating on the electron density we have focused on a quantity that can be accessed directly in experiments. In reference [18] the change of the electron density was probed by measuring the transient currents created on the top electrodes C_1, C_2, G_2 by a periodic change of the density profile induced by an On/Off modulation of the microwave

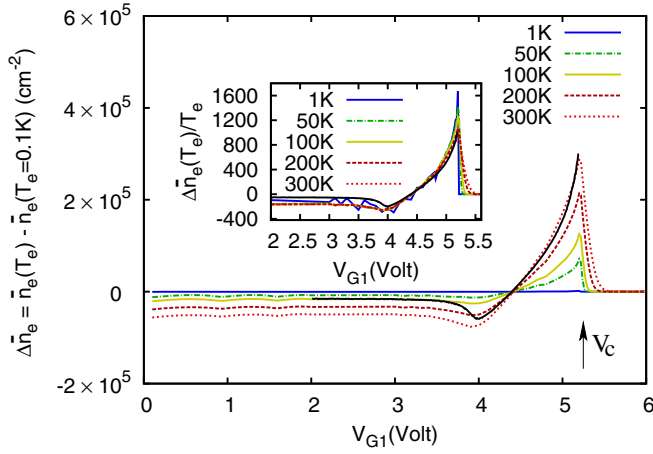


Fig. 3. Electronic density variation $\Delta\bar{n}_e = [\bar{n}(T_e) - \bar{n}(T_e = 0.1\text{ K})]$ as a function of the guard potential V_{G1} for different effective temperatures (from top to bottom at $V_{G1} = 1\text{ V}$: 1 K, 50 K, 100 K, 200 K and 300 K). The plain black curve corresponds to the predictions of the analytic theory equations (11) and (12) at an effective temperature $T_e = 300\text{ K}$. In the inset, the density variation is rescaled by the temperature. For $V_{G1} < V_C$ all curves collapse on each other with a very good agreement with the analytical predictions. For $V_{G1} > V_C$, the scaling breaks down since the photocurrent becomes thermally activated (see discussion in the text). The number of electrons in the cloud was fixed to: $N_e = 10^7$.

power under ZRS conditions. Since the electrodes C_1 and C_2 are held at the same potential $n_e(r)$ is almost constant below these two electrodes, thus a simple plane capacitor model can be used to relate the transient current $i_1(t)$ measured by a current amplifier connected to C_1 and the change in the SE density:

$$i_1(t) = -\frac{e}{2} \frac{d}{dt} \int_{S(C_1)} n_e(\mathbf{r}) d^2\mathbf{r} \quad (4)$$

where $S(C_1)$ denotes the helium surface below the electrode C_1 . Within the frame of our simplified model, the On/Off modulation of the microwave power changes the electron temperature between its equilibrium value $T_0 \simeq 100\text{ mK}$ and its (unknown but possibly several order of magnitude larger) steady state value T_e under illumination. The time-integral of the photo-current during a microwave ON half-cycle will thus be given by:

$$\int i_1(t) dt = -\frac{e}{2} S(C_1) (\bar{n}_e(T_e) - \bar{n}_e(T_0)) \quad (5)$$

where \bar{n}_e denotes the average electron density below the central electrode C_1 . Thus knowing $\Delta\bar{n}_e = \bar{n}_e(T_e) - \bar{n}_e(T_0)$, it is possible to estimate the amount of charge displaced in the experiment. The dependence of $\Delta\bar{n}_e$ on the guard voltage is displayed on Figure 3 for several temperatures T_e .

This figure shows that $\Delta\bar{n}_e$ changes sign as a function of the guard voltage V_{G1} , and exhibits a sharp maximum for V_{G1} close to the transition from a ring to a non-homogeneous disc which occurs at $V_{G1} = V_C$ with

$V_C \simeq 5.21\text{ V}$, this value is obtained from numerical simulations at low temperatures. For potential $V_{G1} < V_B$, a temperature increase causes an expansion of the cloud below the electrode V_{G1} leading to $\Delta\bar{n}_e < 0$. The quantity $\Delta\bar{n}_e$ changes sign at $V_{G1} \simeq V_B = 4.2\text{ V}$ (more precisely at a slightly higher value $V_{G1} \simeq 4.45\text{ V}$) and when the bias voltage $V_{G1} - V_B$ becomes positive we observe $\Delta\bar{n}_e > 0$. We note also that the density change $\Delta\bar{n}_e$ almost vanishes when SE form a ring with a vanishing density in the center at $V_{G1} > V_C$. The latter behavior can be explained with the following argument: at zero temperature when $V_{G1} > V_C$ the potential at the center of the cell is lower than the potential inside the electron ring. This potential difference creates an energy barrier that precludes the electron from exploring the center of the cell when the thermal energy is small compared to the barrier height. The maximal values of $\Delta\bar{n}_e$ are obtained when the electron cloud is in a non-homogeneous disc configuration $V_B < V_{G1} < V_C$. This is intuitively plausible since in this case the center of the cell and the ring are at the same potential at $T_e = 0$ and there is no energy barrier to prevent hot electrons from exploring the center of the cloud. As expected $\Delta\bar{n}_e$ increases with temperature.

The above heuristic arguments can explain the sign of $\Delta\bar{n}_e$ as a function of V_{G1} , but fail to account for some surprising aspects of the functional dependence such as the seemingly non-analytic behavior at $V_{G1} \simeq V_C$. Indeed $\Delta\bar{n}_e(V_{G1})$ features a sharp maximum for $V_{G1} < V_C$, but quickly vanishes at $V_{G1} > V_C$, the asymmetry of this peak becomes even more pronounced at lower T_e . In the next section, we develop a perturbation theory that allows to explain this singularity and its temperature dependence.

2 Perturbative calculation of the effect of temperature

In this section, we derive a simplified analytic theory to explain the behavior of the SE when the electronic temperature is raised from 0 to T_e . At zero temperature, the potential of the electron cloud is fixed and equal to a constant value V_0 . This allows to effectively linearize the equations since the electron cloud can be replaced by an equipotential surface. The boundaries of the cloud are then fixed by the constraint that the electric field vanishes on the boundary (stability condition) and the potential of the cloud V_0 is fixed by the number of electrons in the cloud N_e . Thus the problem of finding the zero temperature density distribution $n_e(r, T = 0)$ is computationally much simpler, and we assume that $n_e(r, T = 0)$ is known in the following derivation.

If the temperature changes, the number of electrons inside the cloud changes by an amount of δn_e , modifying the potential inside the cloud by an amount δV . We assume that the density inside the cloud is just a little perturbed $\delta n_e \ll n_e(r, T_e = 0)$:

$$n_e(r, T_e) = n_e(r, T_e = 0) + \delta n_e(r). \quad (6)$$

Using the Boltzmann-equation, equation (1), we also have:

$$\begin{aligned} n_e(r, T_e) &= n'_{av} \exp\left(\frac{eV_0}{k_B T_e}\right) \exp\left(\frac{e\delta V}{k_B T_e}\right) \\ &= n_{av} \exp\left(\frac{e\delta V}{k_B T_e}\right), \end{aligned} \quad (7)$$

where n_{av} and n'_{av} are normalization constants. Using our assumption $\delta n_e \ll n_e(r, T_e = 0)$ we are led to:

$$n_e(r, T_e = 0) \simeq n_{av} \exp\left(\frac{e\delta V}{k_B T_e}\right) \quad (8)$$

or equivalently:

$$e\delta V = k_B T_e [\log n_e(r, T = 0) - \log n_{av}]. \quad (9)$$

The quantity δV can be estimated in an other way; in the center of the electron cloud where the density is uniform, the variation of density δn_e leads to a change in the potential δV :

$$\delta n_e = -\frac{2\epsilon_0 \delta V}{e h}, \quad (10)$$

this expression just comes from the electrostatics of a planar capacitor. The value of δn_e taken at the center of the cell is equal to $\Delta \bar{n}_e$, eliminating δV between equations (9) and (10), we obtain the following relation

$$\Delta \bar{n}_e = \frac{2\epsilon_0 k_B T_e [\log n_e(r = 0, T = 0) - \log n_{av}]}{e^2 h}. \quad (11)$$

This equation is accurate only in the center of the electron cloud where density gradients can be neglected. Outside the electron cloud, the density decays exponentially with the temperature and can be neglected. If we tentatively assume that equation (11) is valid in the entire cloud, we can find n_{av} from the requirement of the conservation of electron number: $\int \delta n_e r dr = 0$, leading to:

$$\log n_{av} = \frac{\int_{cloud} \log[n_e(r, T = 0)] r dr}{\int_{cloud} r dr}. \quad (12)$$

The integral in this expression is performed for the electron density at $T = 0$ for which the limits of the cloud are well defined.

The combination of equations (11) and (12) allows to find the variation of the electron density at the center of the cell based on the knowledge of the electron density at $T = 0$, they also imply that $\Delta \bar{n}_e$ scales linearly with the temperature T_e (we assume T_e is much larger than the helium bath temperature T_0). The above analysis is justified only for $V_G < V_C$ where the density $n_e(r = 0, T = 0)$ is non vanishing, we have thus compared our semi-analytical theory with the simulations only in this domain. The results are displayed on Figure 3, and show that our semianalytical approach is very successful for $V_G \simeq V_C$ where it reproduces the numerical results

with very good accuracy without any adjustable parameters. The agreement is worse in the limit $V_G \ll V_B$ probably because our assumption that equation (11) is valid in the entire cloud does not hold anymore when the electrons are strongly confined by the guard electrodes. The scaling $\Delta \bar{n}_e \propto T_e$ is also confirmed by the simulations as it is illustrated in the inset of Figure 3. To summarize the proposed theory seems to explain quantitatively the change of the electron density under heating, and allows detailed comparison with numerical simulations and hopefully future experiments.

3 Effect of heating on transport measurements

In previous sections we have investigated the effect of an elevated out of equilibrium temperature on the distribution of the electrons on the helium surface. The information on electron density can be accessed through photo-current measurements similar to those performed in reference [18]. However the most wide-spread type of experiments on SE is a Sommer-Tanner technique which allows to determine the electron longitudinal mobility μ_{xx} [30]. We have thus analyzed numerically the effect of T_e on the outcome of such experiments.

In a Sommer-Tanner measurement an A.C. potential $V_{ac} \cos \omega t$ is applied to one of the top electrodes (we have taken this electrode to be C_1 in our simulations) and the induced AC displacement of image-charges is detected from the remaining ones using a lock-in technique. Our numerical approach to simulate this experiment was a direct numerical integration of the time dependent drift-diffusion equations:

$$\frac{\partial n_e}{\partial t} + \frac{\mu_{xx}}{r} \frac{\partial}{\partial r} \left(r n_e \frac{\partial V}{\partial r} - \frac{k_B T}{e} r \frac{\partial n_e}{\partial r} \right) = 0. \quad (13)$$

This equation is coupled to a Laplace equation on the electrostatic potential, which includes the electron density and the static and time dependent potentials on the electrodes as a boundary conditions. The drift-diffusion equations were integrated using an implicit first order integration scheme solved with a finite element method (FEM). For reference we give here the weak formulation of the differential equation connecting $n_e(r, t + \Delta)$ and $n_e(r, t)$ in our numerical calculations:

$$\begin{aligned} \frac{1}{\mu_{xx}} \int [n_e(r, t + \Delta t) - n_e(r, t)] u(r) r dr = \\ \int \left(n_e(r, t + \Delta t) \frac{\partial V}{\partial r} \frac{\partial u}{\partial r} - \frac{k_B T}{e} \frac{\partial n_e(r, t + \Delta t)}{\partial r} \frac{\partial u}{\partial r} \right) r dr. \end{aligned} \quad (14)$$

The potentials are evaluated at time t and recomputed at time $t + \Delta t$ (Δt is our integration time step) using the updated value of the density n_e , $u(r)$ denotes a finite element trial function. Finite element simulations were performed

using the FreeFem programming language¹, for typical parameters

$$N_e = 3 \times 10^6, \quad V_B = 4.2 \text{ V}, \quad V_{G1} = V_{G2} = 0 \text{ V}.$$

The AC potential with amplitude $V_{ac} = 3 \text{ mV}$ was applied to the electrode C_1 , and the modulation of the image-charge number was determined on the neighboring electrode C_2 after subtraction of the direct capacitive coupling. This modulation $Q(t)$ was separated into in-phase and out of phase components: Q_x and Q_y which respectively denote the amplitude of the $\cos \omega t$ and $\sin \omega t$ components in the total signal $Q(t)$. An immediate consequence of equation (13) is that the quantities Q_x and Q_y depend only on the ratio $\frac{\omega}{\mu_{xx}}$, this is a consequence of the fact that the potentials react instantaneously to the displacement of charges at the typical experimental frequencies in the kHz range. This quantity should then be compared with the parameters of the electron cloud, which for a monotonic disc density distribution are the density at the cloud center n_e and the cloud radius R_c . These considerations lead us to define the dimensionless parameter $W = \frac{\epsilon_0 \omega R_c}{\mu_{xx} e n_e}$ which characterizes the ratio between the frequency and the response time of SE.

We summarized our numerical results in a Cole-Cole diagram that displays trajectories followed by Q_x and Q_y on (Q_x, Q_y) plane as the measurement frequency ω is varied at fixed T_e . At low frequencies when $W \ll 1$ the electrons have time to follow the time varying potential adiabatically and all the displaced image-charge is in phase with the excitation $Q_x \gg Q_y$. As frequency increases, an out of phase component appears since the electrons are unable to respond fast enough to follow the phase of the external potential. Finally at frequencies much higher than the electron characteristic response time $W \gg 1$ their response vanishes and the trajectory converges to the origin ($Q_x = 0, Q_y = 0$).

The simulation results at different temperatures are shown on Figure 4, the obtained trajectories in the (Q_x, Q_y) plane are very similar to semicircles. As the temperature is increased the radius of the semicircle tends to shrink, qualitatively this occurs because some of the terminally excited electrons are not sensitive to the applied bias potential. As a consequence the shape of the trajectories in the (Q_x, Q_y) plane, are very different if the mobility of the electrons changes under microwave irradiation or their temperature. Indeed when μ_{xx} is changed the points (Q_x, Q_y) still collapse on their semi-circular trajectory because it is parameterized only by the ratio $\frac{\omega}{\mu_{xx}}$. On the contrary, when the temperature changes the points (Q_x, Q_y) lie on different semicircles which leads to very different trajectories. An example of a trajectory versus temperature at fixed $\omega/\mu_{xx} = 2 \text{ cm}^2/\text{V}$ is shown Figure 4. Thus heating can create deviations of the (Q_x, Q_y) trajectories from the behavior that would be expected if only the electron mobility changed under microwave irradiation. A possible physical explanation for this reduction of the diameter of semi-circle can be that excitation

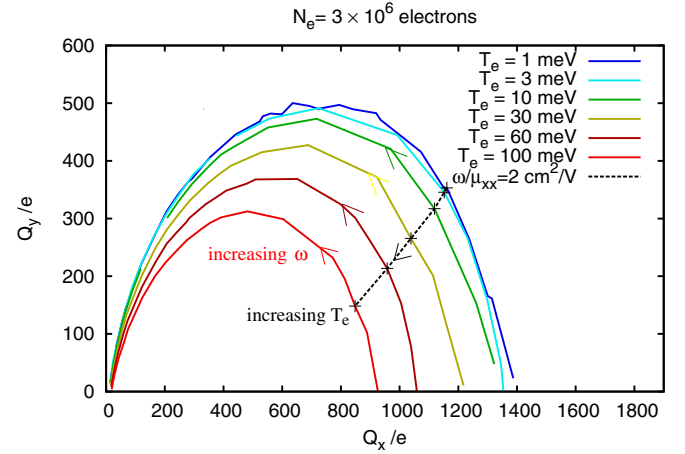


Fig. 4. Cole-Cole diagram of the in-phase (Q_x) and out-of-phase (Q_y) charge modulation on electrode C_2 as the modulation frequency ω is changed and a AC potential with a 3 mV amplitude is applied on C_1 . The charge modulation due to the direct capacitive coupling between both electrodes was subtracted. Continuous curves were obtained at different temperatures that are indicated in the legend (as temperature increases the semicircle radius decreases), the direction of increasing ω (decreasing μ_{xx}) is indicated by the arrows on the curves. The dashed curve with symbols joins points at different temperatures for a fixed value of $\omega/\mu_{xx} = 2 \text{ cm}^2/\text{V}$.

voltages comparable with the electron temperature will not produce a noticeable change in the electron density thereby reducing effectively the radius of the semi-circle on the Cole-Cole diagram. More detailed numerical investigations of the dependence on the AC bias amplitude are needed to understand this behavior quantitatively.

4 Conclusions

We investigated the effect of an elevated out of equilibrium electron temperature on the distribution of surface electrons on liquid helium in a typical experimental geometry. Our main result is probably the determination of the photocurrent induced by an increase of the electron temperature under irradiation. This was achieved numerically by developing a Monte-Carlo method capable of computing the electron density even in the limit of very low temperatures, and analytically through a perturbation theory analysis of the effects of temperature. The dependence of the photocurrent on the control gate voltage that is predicted within our model is quite specific and should provide a reliable signature of electron heating, against other mechanisms possibly at play. Namely we predict that the photocurrent generated by density variation at the center of the cloud changes sign as a function of the guard voltage and is stronger in the reverse bias configuration. Unexpectedly, we also find that the photo-current is maximal when center of the electron cloud is almost depleted. Finally we have also demonstrated numerically that in Sommer-Tanner experiments,

¹ The Freefem simulation and its documentation are available at: <http://www.freefem.org/ff++/index.htm>

heating should induce trajectories on the Cole-Cole diagram that differ strongly from those expected from a change in electron mobility. This could be checked in transient conductance measurements, where the trajectory on the Cole-Cole plane can be measured as the system is driven in and out of a zero resistance state by an on/off modulation of the microwaves power. We hope that our results will allow a quantitative analysis of the electron energy distribution under zero-resistance conditions, and that the analytical and numerical methods developed here will be useful in other systems that are described by a Poisson-Boltzmann equation.

We are thankful to E. Trizac, D. Konstantinov and K. Kono for fruitful discussions. One of us, A.C. acknowledges the support from RIKEN and St Catharine college in Cambridge.

Appendix

In this Appendix, the electrode potential $V_{ext}(\mathbf{r})$ and the Green function $G(\mathbf{r}, \mathbf{r}')$ are calculated. The total potential $V(\mathbf{r})$ is the sum of the electrode potential $V_{ext}(\mathbf{r})$ and the contribution coming from the electrons $V_e(r) = \int G(\mathbf{r}, \mathbf{r}') n_e(\mathbf{r}') d^3\mathbf{r}'$. The cylindrical symmetry of the system allows us to write the different potential as functions of the cylindrical coordinate $\mathbf{r} = (r, \theta, z)$ but we also make use the Eulerian coordinate $\mathbf{r} = (x, y, z)$. Note that in our notations $\|\mathbf{r}\| \neq r$.

Appendix A: Electrode potential $V_{ext}(\mathbf{r})$

The electrode potential $V_{ext}(\mathbf{r})$ is solution of the Poisson equation

$$\Delta V_{ext} = 0. \quad (\text{A.1})$$

Taking the xy -Fourier transform of this equation (A.1), we get:

$$\partial_{zz} \tilde{V}_{ext} - k^2 \tilde{V}_{ext} = 0 \quad (\text{A.2})$$

where $k^2 = k_x^2 + k_y^2$, $\mathbf{k} = (k_x, k_y)$ and

$$V_{ext}(\mathbf{r}) = \iint \frac{d^2\mathbf{k}}{2\pi} e^{i\mathbf{k}\cdot\mathbf{r}} \tilde{V}_{ext}(\mathbf{k}, z). \quad (\text{A.3})$$

The solution of equation (A.2) are

$$\tilde{V}_{ext}(k_x, k_y, z) = A(k_x, k_y) \cosh(kz) + B(k_x, k_y) \sinh(kz) \quad (\text{A.4})$$

where $A(k_x, k_y)$ and $B(k_x, k_y)$ are functions which satisfy the bordering conditions. The cylindrical symmetry imposes $A(k_x, k_y) = A(k)$ and $B(k_x, k_y) = B(k)$, leading to:

$$V_{ext}(r, \theta, z) = \int_0^\infty k dk J_0(kr) [A(k) \cosh(kz) + B(k) \sinh(kz)], \quad (\text{A.5})$$

where $J_i(x)$ is the i th Bessel function of the first kind. Quoting V_i the potential of the electrode i , R_i the maximal radius of the electrode i and $H(r < R_i)$ the Heaviside function (equal 1 if the argument is true, else zero), the electrode potential has to respect the following boundary conditions:

$$V_{ext}(r, z = h) = V_{G_2} [H(r < R_{G_2}) - H(r < R_{C_2})] \quad (\text{A.6})$$

$$V_{ext}(r, z = -h) = V_B H(r < R_B) + V_{G_1} [H(r < R_{G_1}) - H(r < R_B)]. \quad (\text{A.7})$$

It is straightforward to calculate

$$H(r < R) = \int_0^\infty R J_1(kR) J_0(kr) dk. \quad (\text{A.8})$$

From equations (A.6)–(A.8), we obtain the following boundary conditions:

$$\begin{aligned} V_{ext}(r, h) &= \int_0^\infty J_0(kr) V_{G_2} [R_{G_2} J_1(kR_{G_2}) - R_{C_2} J_1(kR_{C_2})] dk \\ &= \int_0^\infty k J_0(kr) [A(k) \cosh[kh] + B(k) \sinh[kh]] dk \\ V_{ext}(r, -h) &= \int_0^\infty J_0(kr) [(V_B - V_{G_1}) R_B J_1(kR_B) + V_{G_1} R_{G_1} J_1(kR_{G_1})] dk \\ &= \int_0^\infty k J_0(kr) [A(k) \cosh[kh] - B(k) \sinh[kh]] dk. \end{aligned}$$

Which leads to:

$$A(k) = \frac{1}{2k \cosh[kh]} [V_{G_2} [R_{G_2} J_1(kR_{G_2}) - R_{C_2} J_1(kR_{C_2})] + (V_B - V_{G_1}) R_B J_1(kR_B) + V_{G_1} R_{G_1} J_1(kR_{G_1})], \quad (\text{A.9})$$

$$B(k) = \frac{1}{2k \sinh[kh]} [V_{G_2} [R_{G_2} J_1(kR_{G_2}) - R_{C_2} J_1(kR_{C_2})] - (V_B - V_{G_1}) R_B J_1(kR_B) - V_{G_1} R_{G_1} J_1(kR_{G_1})]. \quad (\text{A.10})$$

With these expressions of $A(k)$ and $B(k)$, the electrode potential $V_{ext}(r)$ is completely determined.

Appendix B: Electron potential $V_e(\mathbf{r})$

Lets us consider an electron in the center of the system, that means localized at the coordinate $(0, 0, 0)$. This

electron creates a potential $V_e(\mathbf{r})$. This potential can be written

$$V_e(\mathbf{r}) = -\frac{e}{4\pi\epsilon_0} \left(\frac{1}{\|\mathbf{r}\|} + \bar{V} \right). \quad (\text{B.1})$$

The term $1/\|\mathbf{r}\|$ is coming from the solution of the Laplace equation for a pointlike charge and the term \bar{V} , solution of the Laplace equation $\Delta\bar{V} = 0$, permits at the potential to satisfy the boundary conditions $V_e(r, \theta, z = \pm h) = 0$. As previously, the potential \bar{V} can be obtained as, see equation (A.5):

$$\begin{aligned} \bar{V}(r, z) = & \int_0^\infty k dk J_0(kr) [\bar{A}(k) \cosh(kz) \\ & + \bar{B}(k) \sinh(kz)]. \end{aligned} \quad (\text{B.2})$$

The function $\bar{B}(k)$ must be equal to 0 due to the symmetry of the problem. Furthermore, we can calculate

$$\frac{1}{\|\mathbf{r}\|} = \int k J_0(kr) \frac{e^{-k|z|}}{k} dk, \quad (\text{B.3})$$

leading to the full electronic potential $V_e(r, z)$:

$$\begin{aligned} V_e(r, z) = & \frac{-e}{4\pi\epsilon_0} \int_0^\infty k J_0(kr) \\ & \times \left[\bar{A}(k) \cosh[kz] + \frac{e^{-k|z|}}{k} \right] dk. \end{aligned} \quad (\text{B.4})$$

The boundary conditions $V_e(r, z = \pm h) = 0$ lead to the following expression for $\bar{A}(k)$:

$$\bar{A}(k) = -\frac{e^{-kh}}{k \cosh[kh]}, \quad (\text{B.5})$$

and then

$$V_e(\rho, z) = \frac{-e}{4\pi\epsilon_0} \int_0^\infty J_0(k\rho) \left[e^{-k|z|} - e^{-kh} \frac{\cosh[kz]}{\cosh[kh]} \right] dk. \quad (\text{B.6})$$

Appendix C: The complete potential $V(\mathbf{r})$

To obtain the complete potential due to all electrons and electrodes, we have to sum the electrode potential and the potential created by the surface electrons distributed with a density $n_e(r)$ in the plan $z = 0$:

$$V(r, z) = V_{ext}(r, z) + \int_0^{R_c} \int_0^{2\pi} V_e(\|\mathbf{r} - \mathbf{r}'\|, z) n_e(r') r' dr' d\theta. \quad (\text{C.1})$$

Now, we have to note that the electrons can move only in the plan $z = 0$ and, by this fact, the electrons feel a potential $V(r, z = 0) \equiv V(r)$ defined by:

$$\begin{aligned} V(r) = & V_{ext}(r, z = 0) - \frac{e}{2\epsilon_0} \int_0^\infty dk \tanh[kh] \\ & \times \int_0^{R_c} dr' r' J_0(kr) J_0(kr') n(r'). \end{aligned} \quad (\text{C.2})$$

The comparison between equations (C.2) and (2) gives the following expression for the Green function

$$G(r, r') = \frac{-e}{4\pi\epsilon_0} \int_0^\infty dk \tanh[kh] J_0(kr) J_0(kr'). \quad (\text{C.3})$$

The full potential $V(r)$, see equation (C.2), is numerically obtained. In order to increase the numerical precision, the integrations are done successively between two consecutive zeros of the Bessel functions $J_0(kr)$ or $J_0(kr')$.

References

1. *Electrons on Helium and Other Cryogenic Substrates*, edited by E.Y. Andrei (Kluwer Academic, Dordrecht, 1997)
2. Y. Monarkha, K. Kono, *Two-Dimensional Coulomb Liquids and Solids* (Springer, Berlin, 2004)
3. G.C. Grimes, G. Adams, Phys. Rev. Lett. **42**, 795 (1979)
4. D.C. Glattli, E.Y. Andrei, G. Deville, J. Poitrenaud, F.I.B. Williams, Phys. Rev. Lett **54**, 1710 (1985)
5. V.A. Volkov, S.A. Mikhailov, in *Landau Level Spectroscopy* (Elsevier Science Publ., North-Holland, 1991), p. 855
6. D.G. Rees, I. Kuroda, C.A. Marrache-Kikuchi, M. Höfer, P. Leiderer, K. Kono, Phys. Rev. Lett. **106**, 026803 (2011)
7. A.V. Smorodin, V.A. Nikolaenko, S.S. Sokolov, L.A. Karachevtseva, O.A. Lytvynenko, Low Temp. Phys. **38**, 915 (2012)
8. T. Günzler, B. Bitnar, G. Mistura, S. Nesper, P. Leiderer, Surf. Sci. **361-362**, 831 (1996)
9. K. Shirahama, K. Kono, Phys. Rev. Lett. **74**, 781 (1995)
10. K. Shirahama, K. Kono, J. Low Temp. Phys. **104**, 237 (1996)
11. D.I. Schuster, A. Fragner, M.I. Dykman, S.A. Lyon, R.J. Schoelkopf, Phys. Rev. Lett. **105**, 040503 (2010)
12. G. Papageorgiou, P. Glasson, K. Harrabi, V. Antonov, E. Collin, P. Fozooni, P.G. Frayne, M. Lea, D.G. Rees, Y. Mukharsky, Appl. Phys. Lett. **86**, 153106 (2005)
13. F.R. Bradbury, M. Takita, T.M. Gurrieri, K.J. Wilkel, K. Eng, M.S. Carroll, S.A. Lyon, Phys. Rev. Lett. **107**, 266803 (2011)
14. D. Konstantinov, M.I. Dykman, M.J. Lea, Yu.P. Monarkha, K. Kono, Phys. Rev. Lett. **103**, 096801 (2009)
15. D. Konstantinov, K. Kono, Phys. Rev. Lett. **105**, 226801 (2010)
16. R.G. Mani, J.H. Smet, K. von Klitzing, V. Narayanamurti, W.B. Johnson, V. Umansky, Nature **420**, 646 (2002)
17. M.A. Zudov, R.R. Du, L.N. Pfeiffer, K.W. West, Phys. Rev. Lett. **90**, 046807 (2003)
18. D. Konstantinov, A.D. Chepelianskii, K. Kono, J. Phys. Soc. Jpn **81**, 093601 (2012)
19. A.D. Chepelianskii, D.L. Shepelyansky, Phys. Rev. B **80**, 241308(R) (2009)
20. O.V. Zhirov, A.D. Chepelianskii, D.L. Shepelyansky, Phys. Rev. B **88**, 035410 (2013)
21. Y.P. Monarkha, Low Temp. Phys. **37**, 655 (2011)
22. Y.P. Monarkha, Low Temp. Phys. **38**, 451 (2012)
23. I.A. Dmitriev, A.D. Mirlin, D.G. Polyakov, M.A. Zudov, Rev. Mod. Phys. **84**, 1709 (2012)

24. D. Konstantinov, H. Isshiki, H. Akimoto, K. Shirahama, Y. Monarkha, K. Kono, J. Phys. Soc. Jpn **77**, 034705 (2008)
25. A. Chepelianskii, F. Mohammad-Rafiee, E. Trizac, E. Raphael, J. Phys. Chem. B **113**, 3743 (2009)
26. A.D. Chepelianskii, F. Closa, E. Raphaël, E. Trizac, Eur. Phys. Lett. **94**, 68010 (2011)
27. L. Wilen, R. Giannetta, J. Low Temp. Phys. **72**, 353 (1988)
28. Y.Z. Kovdrya, V.A. Nikolayenko, O.I. Kirichek, S.S. Sokolov, V.N. Grigor'ev, J. Low Temp. Phys. **91**, 371 (1993)
29. F. Closa, A.D. Chepelianskii, E. Raphaël, E. Trizac, to be published
30. W.T. Sommer, D.J. Tanner, Phys. Rev. Lett. **27**, 1345 (1971)